IEEE Access
Multidisciplinary ⋮ Rapid Review ⋮ Open Access Journal

Received March 1, 2022, accepted March 19, 2022, date of publication March 30, 2022, date of current version April 7, 2022.

Digital Object Identifier 10.1109/ACCESS.2022.3163303

Planar Ultrawideband Circularly Polarized Cosine Slot Archimedean Spiral Antenna for Partial Discharge Detection

YUGANDHARA RAO YADAM[1], RAMANUJAM SARATHI[2], (Senior Member, IEEE), AND KAVITHA ARUNACHALAM[1], (Member, IEEE)

[1]Department of Engineering Design, Indian Institute of Technology Madras, Chennai 600036, India
[2]Department of Electrical Engineering, Indian Institute of Technology Madras, Chennai 600036, India

Corresponding author: Kavitha Arunachalam (akavitha@iitm.ac.in)

This work was supported by the Central Power Research Institute (CPRI), India, under Grant CPRI/R&D/TANS/2019.

ABSTRACT Design and experimental verification of an ultrawideband planar circularly polarized ultrahigh frequency (UHF) sensor is presented for detection of partial discharge (PD) activities in high voltage (HV) equipment. The proposed sensor is cavity-backed cosine slot Archimedean spiral (CSAS) antenna with an electromagnetic (EM) transparent radome. The dual-arm slot spiral was meandered as cosine wave for size reduction and optimized for broadband operation with circular polarization (CP) over 0.5-5 GHz. Unidirectional radiation pattern with CP was achieved over 0.5-5 GHz using an optimized cavity loaded with EM absorber. The fabricated UHF CSAS sensor has the widest operating bandwidth of 0.5-5 GHz with circular polarization and the smallest aperture of $0.26\lambda_L$ when compared to the existing UHF PD sensors, where λ_L is the wavelength at the lowest operating frequency. Time domain incipient discharge signals and phase resolved PD patterns gathered for three commonly occurring defects in test cells mimicking gas insulated switchgear (GIS) indicate better sensitivity and detection capability for the fabricated CSAS UHF sensor than the reference PD sensor. PD signal measurements and comparison with other UHF PD sensors indicate that the proposed UHF CSAS sensor could be used for PD detection in HV equipment.

INDEX TERMS Circular polarization, high voltage, gas insulated switchgear, partial discharge, spiral antenna, ultrawideband, ultrahigh frequency.

I. INTRODUCTION

Continuous detection and monitoring of partial discharges in high voltage (HV) electrical equipment is essential to avoid reaching the breakdown state of the insulation so that life time of the equipment can be enhanced. Gas insulated switchgear (GIS) is gaining considerable importance in recent times due to its ability to transmit high power in limited space [1]. Partial discharges (PDs) occur in high voltage GIS equipment due to sharp protrusions, free metallic particles, and voids in spacers which are created during production, transportation and installation [2]. PDs can be detected using acoustic, optical, chemical and ultrahigh frequency (UHF) sensing methods [3]. Among all methods, UHF sensing technique is popular due to its ability to detect all types of PDs, ease of installation, and suitability for online condition monitoring in GIS [4]–[6]. Several types of UHF sensors were used such as Hilbert antenna [7], slot antenna [8], spiral antenna [9], [10], disc sensor [11], and monopole antenna [12] were reported for PD detection.

Among the UHF PD sensors, spirals have the advantages of low profile, wide bandwidth (BW), good gain and circular polarization [10]. Among the spiral antennas, Archimedean spiral antenna (ASA) is widely used as it exhibits circular polarization over wider frequency band than the log spiral, but it has relatively large aperture area. The UHF spiral antennas reported for PD detection have large aperture ($\geq$ 200 mm) [9], [10], [13]–[15] which limit their use as internal UHF sensor in GIS or window sensor in power transformers. Besides the large aperture size, axial ratio which is an indicator of antenna's circular polarization has not been presented for the UHF spiral sensors widely reported

The associate editor coordinating the review of this manuscript and approving it for publication was Pavlos I. Lazaridis.

in literature for PD detection [9], [13]–[17]. The circularly polarized ASA reported for PD detection has narrow operating bandwidth of 0.7 to 1.6 GHz and PD detection capabilities were not demonstrated [10]. UHF spiral sensors with bi-directional radiation pattern reported for PD detection [9], [13] are susceptible to ambient EM interference. The quarter wave metal cavity corresponding to the lowest operating frequency yield unidirectional radiation pattern at the cost of high axial ratio and narrow operating bandwidth. The balanced-unbalanced (balun) transmission line used to feed the spiral arms is a delicate structure which further increases the antenna dimensions [10], [13]–[18]. Several of the UHF spiral sensors lack the protective radome which provides electrical isolation from the HV environment [7], [9]–[11], [13]–[18]. Lastly, PD detection capability and sensitivity have not been demonstrated for several UHF spiral sensors reported for PD detection [10], [11], [13], [17]. Thus, spiral antennas reported for PD detection have large aperture and do not possess ultrawideband operation, unidirectional radiation pattern and circular polarization in the UHF range which are desirable for PD detection due to multi-path propagation and EM interference in the HV environment.

There are several ways to miniaturize the ASA [19]–[21]. One such way is to meander its arms, which increases the electrical length of spiral arms. As meandering decreases the outer radius of the spiral, lowering of operating frequency was reported with periodic Z plane meandering [19]. Spiral arms with rectangular wave meandering at the end, full rectangular wave meandering and saw tooth wave meandering were also proposed for broadband operation and miniaturization [20]. Recently, numerical simulations of cosine wave meandered ASA operating over 0.92 – 3 GHz was reported for PD detection [22] with an wideband balun feed for symmetric bi-directional radiation from two electrically conductive spiral arms. This simulation study did not present PD detection capability or free space measurements of the meandered ASA.

Knowing these limitations of UHF PD sensors, we present a miniaturized planar ultrawideband circularly polarized UHF spiral antenna for PD detection with unidirectional radiation pattern. The proposed UHF PD sensor is cosine slot Archimedean spiral antenna (CSASA) optimized with a protective radome. Instead of metal spiral arms, we present a pair of planar slot spiral on the ground plane of 1.6 mm thick dielectric substrate. The planar slot spiral arms are center fed on the back plane of the dielectric substrate using aperture coupling. This type of feeding has advantages of broad bandwidth and low cross polarization. Furthermore, it eliminates the need for a wideband unbalanced to balanced transition typically used to feed the dual arms of the planar slot antenna. Thus, a simplified feed design is proposed unlike the large and delicate ultrawideband balun. The cavity backing of the UHF CSASA loaded with EM absorber is optimized for circular polarization over ultrawideband frequency of 0.5-5 GHz. The optimized CSASA design is fabricated and experimentally verified for its radiation characteristics in free space. The PD detection capability and sensitivity of the fabricated UHF CSASA sensor were assessed using GIS test cells with Corona, particle movement and surface discharge type of PD defects. The PD measurements were compared with conventional UHF PD sensor and its free space radiation characteristics were compared with existing UHF spiral antenna-based PD sensors.

The organization of the paper is as follows: The proposed UHF sensor design and optimization are presented in Section II. The optimized sensor fabrication and free space characteristics are presented in Section III. PD detection capability of the fabricated sensor and its comparison with reference UHF PD sensor are presented in Section IV followed by conclusion Section V.

II. UHF SENSOR DESIGN AND OPTIMIZATION

A. SENSOR DESIGN

Figure 1 shows the cavity backed CSASA with radome investigated in this work. The outer diameter of the antenna determines the lower operating frequency, while the inner diameter determines the upper operating frequency. The slotted arms of spiral were meandered as cosine wave to reduce the antenna aperture size. The slot was defined as,

$$r = r_0 + a\phi + m\left(\frac{\phi - \phi_{st}}{\phi_{end} - \phi_{st}}\right)\cos(n\phi)\,. \tag{1}$$

by adding cosine function to the Archimedean parametric equation. In Eqn. (1), r_0 is the initial radius of the spiral, a is the spiral growth rate, ϕ is the spiral angle that is varied from the starting angle ϕ_{st} to the ending angle ϕ_{end}, and m and n are the amplitude and angular frequency of the cosine wave, respectively. The equation defines one edge of the slot and the other edge was obtained by rotating equation-based curve by 90°. The second arm was obtained by rotating the first slot by 180°. The ends of slots were tapered gradually to minimise reflections arising due to abrupt truncation. The slot spiral is a complimentary structure of the patch spiral antenna, which is obtained by interchanging the conductive material and air regions. In Figure 1(a), the black region denotes the antenna ground plane etched on copper cladded dielectric substrate and white space denotes air column above the substrate. A superstrate of thickness S_w with dielectric property same as the substrate was used to improve antenna impedance matching and gain. The CSASA was centre fed using aperture coupling from microstrip transmission line on the back side of the substrate. The microstrip transmission line was placed perpendicular to the slot at the centre of the dual arms of the CSASA such that the electric field lines from the microstrip line excited tangential electric field in the slot opening. For efficient excitation of the slot, the microstrip transmission line was short-circuited immediately after coupling the electric field to the CSASA. Thus, the aperture coupled feed maintained tangentially oriented electric field with nearly uniform field strength over a wide frequency band. A miniaturized coaxial cable with sub-miniature interface and snap-on mating was used to realize the feed as shown in

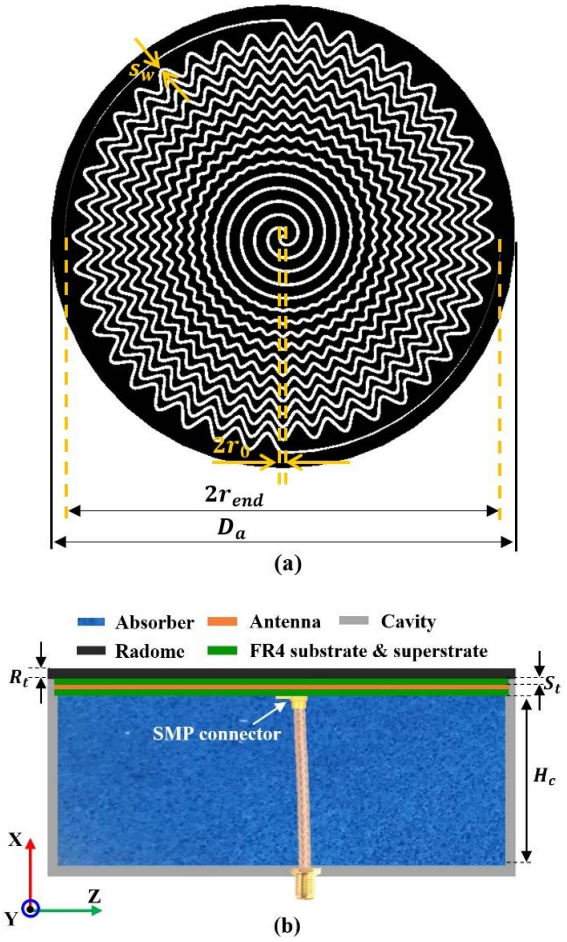

FIGURE 1. Illustration of the ultrawideband cavity backed UHF cosine slot spiral Archimedean antenna (CSASA) sensor for PD detection. (a) Slotted metal plane in which the black region is metal and white space is air, (b) cross sectional view.

Figure 1(b). The snap-on sub-miniature interface was chosen as it occupies very less space which is essential to realize the low-profile aperture coupled feed at the centre of the CSASA.

B. NUMERICAL MODELLING

The antenna was modelled in electromagnetic (EM) simulation software, Ansys HFSS® (Ansys Corp., USA). The substrate and superstrate were assigned the material properties of FR4 laminate. The substrate thickness was 1.6 mm and the copper cladding was set as 17 μm. The slot pattern in Figure 1(a) was etched on the substrate and the antenna was fed using a microstrip transmission line connected to a sub-miniature SMP coaxial connector (Amphenol, USA) as shown in Figure 1(b). An air box of size $\lambda_L/2$ corresponding to the low frequency of 0.5 GHz was defined around the antenna to confine the computational domain. Radiation boundary condition was defined on the faces of the air box to mimic free space and absorb the outgoing waves incident on it. Table 1 lists the material properties used in the simulations. The ground plane, microstrip transmission line and conductive parts of the coaxial connector were assigned as perfect electric conductor. A swept frequency simulation from 0.5 to 5 GHz with 0.05 GHz frequency stepping was defined as the excitation. The EM field radiated by the CSASA inside the computation domain was calculated by solving the vector wave equation iteratively.

TABLE 1. Material properties used in simulation.

Component	Material	Relative permittivity	Loss tangent
Substrate/superstrate	FR4	4.4	0.02
Enclosing domain	Air	1	0
Radome	ABS plastic	3.1	0.0051

C. DESIGN OPTIMIZATION

CSASA design optimization was initially carried out only for the antenna design parameters namely, inner radius (r_0), spiral growth rate (a), outer radius (r_{end}), slot width (S_w), amplitude of cosine wave (m), and superstrate thickness (S_t) without the cavity and radome. Once the antenna parameters were optimized, radome and cavity were included for final design optimization. The CSASA antenna dimensions were optimized for wideband operation with at least 10 dB input return loss ($-20\log_{10}|S_{11}|$) i.e., $|S_{11}| \leq -10$ dB over 0.5–5 GHz, where S_{11} is the antenna input voltage reflection coefficient. The inner radius r_0, growth rate a and number of turns N were set as 2.5 mm, 1.29 and 8, respectively based on the theoretical calculations for the ASA [23]. The following values were assigned to the CSASA initially and their respective optimal values were selected using parametric simulations in HFSS: $r_{end} = 55$ mm, $S_w = 1.0$ mm, $m = 2$ mm, and $S_t = 0$ (no superstrate). At a time only one parameter was varied while all other parameters were kept constant.

Firstly, the outer radius r_{end} was varied from 55 to 75 mm in steps of 5 mm to achieve return loss $\geq$10 dB over 0.5 to 5 GHz. Figure 2(a) shows the sensor power reflection coefficient for varying r_{end}. It can be observed that with increase in r_{end}, low frequency performance of the antenna improved while the high frequency performance remained the same up until $r_{end} < 70$ mm. For $r_{end} = 70$ mm, antenna high frequency performance also improved but the overall performance started deteriorating for $r_{end} > 70$ mm. The antenna 10 dB bandwidth for $r_{end} = 70$ mm is 0.5 – 2.3 GHz. Next, the slot width S_w of CSASA was varied from 0.6 to 1.4 mm in steps of 0.2 mm for $r_{end} = 70$ mm, $m = 2$ mm, $S_t = 0$ mm. Figure 2(b) shows the antenna power reflection coefficient for varying slot width S_w. It can be observed that increasing the slot width S_w degrades the low frequency performance and improves the high frequency performance. Slot width of 1.2 mm was chosen as a trade-off between the low and high frequency response with 10 dB operating bandwidth of 0.5 – 2.4 GHz.

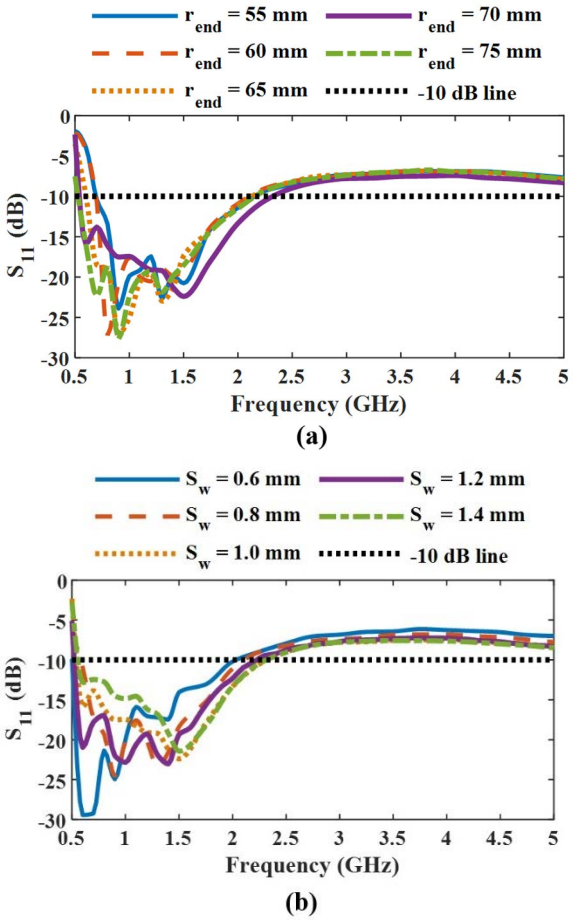

FIGURE 2. Power reflection coefficient of CSASA for varying (a) spiral outer radius r_{end} and (b) slot width S_w.

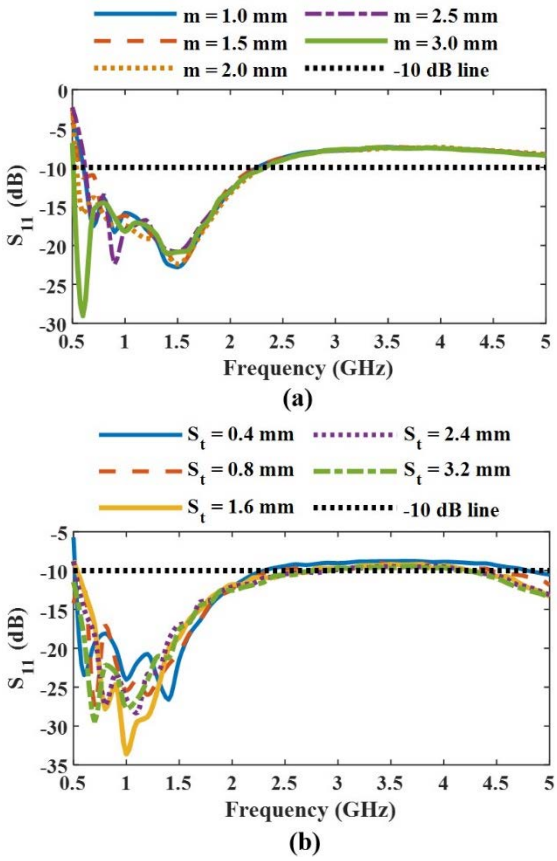

FIGURE 3. Power reflection coefficient of CSASA for varying (a) amplitude of cosine wave meandering m and (b) superstrate thickness S_t.

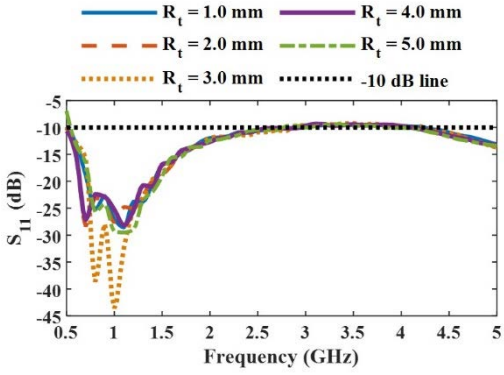

FIGURE 4. Power reflection coefficient of CSASA for varying thickness of radome R_t.

Next, the amplitude of the cosine wave m was varied from 1 to 3 mm in steps of 0.5 mm for $r_{end} = 70$ mm, $S_w = 1.2$ mm, $S_t = 0$ mm. Figure 3(a) shows the antenna power reflection coefficient for varying cosine wave amplitude m. It can be observed that the high frequency performance was not affected for varying m. The antenna performance was the best for $m = 3$ mm. The thickness of the superstrate also affects the antenna performance and it was optimized to improve the antenna impedance matching. The parametric sweep of S_t was limited to the commercially available substrate thickness of FR4 laminate. Figure 3(b) shows the antenna power reflection coefficient for varying S_t, $r_{end} = 70$ mm, $S_w = 1.2$ mm, and $m = 3$ mm. It can be observed that the antenna input power reflection coefficient significantly improved with addition of the superstrate. For $S_t = 1.6$ mm, the antenna return loss $\geq$9.9 dB over an ultrawide frequency of 0.5 – 5 GHz. Thus, ultrawideband operation was realized for the following design parameters: $r_0 = 2.5$ mm, $a = 1.29$, $N = 8$, $r_{end} = 70$ mm, $S_w = 1.2$ mm, $m = 3$ mm, and $S_t = 1.6$ mm. A 5 mm width metal ring was added to the antenna perimeter for securing it to the radome which increased the outer diameter D_a to 150 mm ($2r_{end} + 10$ mm).

The optimized CSASA was covered with ABS plastic radome for electrical isolation of the UHF sensor from HV environment. The radome thickness R_t was varied from 1 to 5 mm in steps of 1 mm. Figure 4 shows the sensor power reflection coefficient for varying radome thickness R_t. The -10 dB bandwidth of the sensor did not change till $R_t = 4$ mm and it started degrading for $R_t \geq 4$ mm. Thus, radome thickness was set as 4 mm to provide electrical isolation and mechanical strength to UHF CSASA sensor.

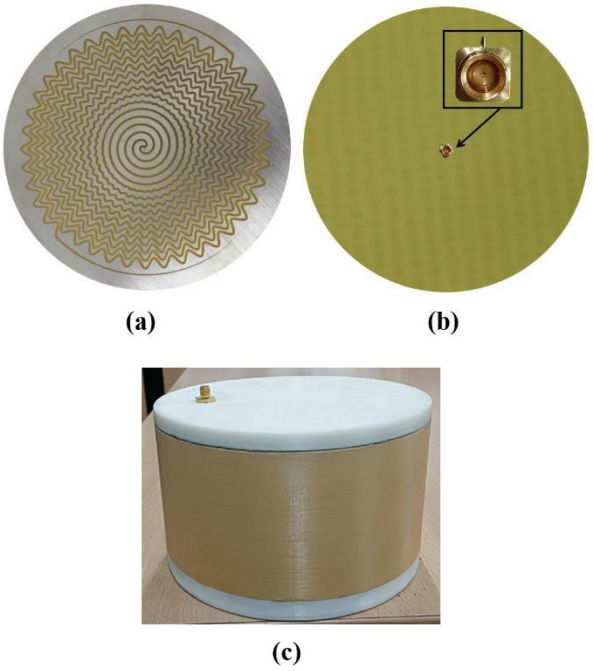

FIGURE 5. Fabricated CSASA sensor showing (a) antenna top view, (b) bottom view and (c) complete assembly of antenna, cavity and radome.

III. SENSOR FABRICATION AND CHARACTERIZATION

A. UHF SENSOR FABRICATION

The UHF CSASA was fabricated on 1.6 mm thick FR4 laminate for the optimized antenna dimensions arrived in Section II using printed circuit board manufacturing process. The top and bottom sides of the fabricated CSASA are shown in Figures 5(a) and 5(b), respectively. The CSASA sensor with the radome has bidirectional radiation pattern as the radome is transparent to EM waves. The radiation pattern was converted to unidirectional radiation pattern using cavity backing in order to minimize EM interference pick up from the environment. An air filled metal cavity of height $H_c = \lambda_L/4$ results in 150 mm tall cavity backing [24]. The resonant cavity design suppresses the back radiation but it also significantly affects the antenna circular polarization and degrades the sensor operating bandwidth. Thus, an ultrawideband cavity was realized empirically to yield circular polarization over the operating bandwidth of 0.5 – 5 GHz by loading the cavity with broadband EM absorber. A 3D printed ABS plastic outer shell plastered with adhesive aluminium tape was used as the metal cavity. The fabricated CSASA antenna with the superstrate and radome was fitted with the metal cavity and the cavity was loaded with commercially procured broadband EM absorber foam of height H_c loaded with conductive carbon particles (JV Micronics, UP, India). The cavity height H_c was varied at the following discrete intervals using an adjustable metal shorting plate: 30, 50, 80, 100, and 150 mm.

Free space radiation measurements of the cavity backed UHF CSASA sensor in an anechoic chamber gathered using vector network analyzer (VNA) (E5071C, Keysight Technologies, USA) for varying H_c were used to determine the least cavity height that yielded axial ratio $AR < 3$ dB and return loss ≥ 10 dB over 0.5 to 5 GHz. Cavity height optimization was carried out empirically as the permittivity and permeability of the EM absorber were not available for our operating bandwidth. Figure 5(c) shows the UHF sensor with the radome and an optimized cavity made of 4 mm thick 3D printed ABS plastic. A miniaturized coaxial cable with SMP surface mount connector soldered on the backside of the antenna substrate was guided through the absorber loaded metal cavity as shown in Figure 5(c). The outer diameter of the UHF CSASA sensor with the radome and cavity backing shown in Figure 5 is 158 mm (D_a+ 8 mm).

B. FREE SPACE MEASUREMENTS

Figure 6 shows the *AR* of the fabricated cavity backed UHF CSASA sensor for varying cavity height H_c measured using a VNA in an anechoic chamber. Measurements were recorded for 32-point averaging and frequency span of 0.5–5 GHz. It can be observed that the $AR < 3$ dB over 0.5–5 GHz for $H_c = 80$ mm. Thus, optimal cavity height and thickness of the EM absorber was set as 80 mm. The UHF CSASA sensor with the optimized absorber filled cavity is shown in Figure 5(c). Figure 7 shows the input power reflection coefficient of the fabricated and simulated circularly polarized CSASA sensor proposed for PD detection. Measurements are also shown for the reference UHF disc sensor used for PD measurements in our laboratory. Simulation results of the CSASA sensor with an air-filled cavity height of 80 mm are also shown in Figure 7 for comparison. It can be observed that the reference UHF sensor measurements have multiple resonances and limited bandwidth, whereas the proposed circularly polarized UHF CSASA sensor measurements have ultrawide bandwidth of 0.5–5 GHz with reflection coefficient < -10 dB. Figure 8 shows the gain measurements of the UHF CSASA sensor. It can be observed that the fabricated UHF sensor has non-zero gain over 0.5 – 5 GHz with peak gain of 4.95 dB at 2.4 GHz. Gain measurements are shown starting from 1 GHz as the lower operating frequency of the standard gain horn (DRH18-E, RFspin Ltd., Czech Republic) is 1 GHz. Antenna gain is a far field property unlike the reflection coefficient which is a measure of the impedance matching between the antenna input terminals and the feed line. The gain is the product of antenna radiation efficiency given by $e_{cd}(1 - |S_{11}|^2)$ and the directivity, where e_{cd} denotes the conductor and dielectric losses associated with the antenna. The high gain observed about 2.45 GHz in Figure 8 indicates that the radiation efficiency and directivity of the antenna is high at 2.45 GHz despite having the minimum return loss in the operating bandwidth.

Figure 9 shows the radiation pattern of the CSASA sensor measured in an anechoic chamber for line-of-sight illumination in XY ($\phi = 0^\circ$; $\theta = -180$ to 180°) and XZ ($\phi = 90^\circ$; $\theta = -180$ to 180°) planes using the standard gain horn. The absorber loaded cavity yielded unidirectional radiation

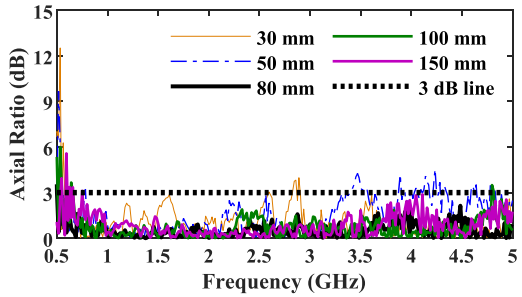

FIGURE 6. Axial ratio of the CSASA sensor for varying cavity height H_c.

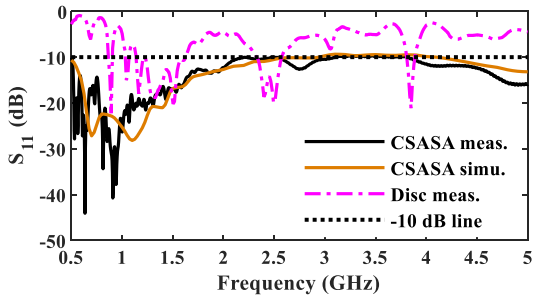

FIGURE 7. Simulated and measured power reflection coefficient of CSASA sensor and its comparison with the reference UHF disc sensor.

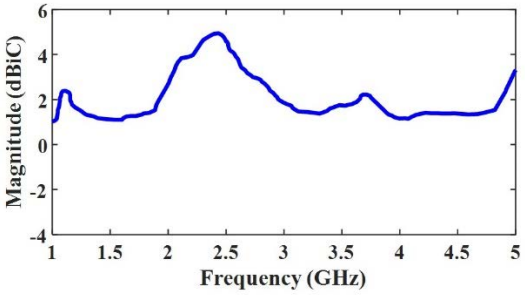

FIGURE 8. Measured gain of the fabricated UHF CSASA sensor in Figure 5.

pattern in the operating bandwidth. The deviation between measurements and simulations in Figure 9 is attributed to sensor fabrication errors and deviation in the 3D printed material property. Sensor free space characterization measurements in Figures 6-9 confirm that the fabricated UHF CSASA sensor has ultrawide bandwidth with $\geq$ 10 dB return loss, circular polarization, positive gain and unidirectional radiation pattern over a wide frequency band of 0.5 – 5 GHz desirable for PD detection.

IV. PD MEASUREMENTS

A. EXPERIMENTAL SETUP

Figure 10(a) shows the laboratory setup used to determine the PD detection capability of the fabricated UHF CSASA sensor. The sensor performance was evaluated for its ability to measure raw PD signals as well as phase resolved PD (PRPD) pattern in an unshielded laboratory environment. The setup consists of function generator, Trek amplifier (Model 20/20C) connected to the SF6 gas filled GIS test cells with three different electrode configurations for simulating PD activities (Figures 10(b)-(d)), reference UHF disc sensor, CSASA sensor, and digital storage oscilloscope (DSO) for raw PD signal acquisition and analysis (Figure 10(e)).

The DSO was replaced with signal analyser for PRPD analysis as illustrated in Figure 10(f). Three types of defects commonly occurring in GIS and other HV equipment namely, Corona (Cor), particle movement (PM), and surface discharge (SD) were simulated using the electrode configurations shown in Figures 10(b)-(d). Corona type of PD was generated using needle shaped HV electrode and flat ground electrode (needle-plane configuration) with 5 mm separation distance as shown in Figure 10(b). PM type of PD was generated using spherical upper electrode and a concave shaped bottom electrode with 5 mm separation distance. A 1 mm diameter aluminium particle was placed on the ground electrode to initiate PM type of discharges as shown in Figure 10(c). SD type of PD was generated by sandwiching 1.5 mm thick epoxy insulating disc between IEC(b) electrode and flat ground electrode as shown in Figure 10(d). The test cells were filled with SF_6 gas maintained at 3 bar. A continuous power frequency (50 Hz) sinusoidal voltage from function generator was delivered to Trek amplifier and its magnitude was increased gradually until PD phenomenon was initiated in the test cell. The minimum voltage at which the PD signals generated is called inception voltage. The inception voltage was increased by 10% for the respective minimum value for all PD defect types so that the PD signals can be detected with good strength by both UHF sensors.

The radiated PD signals from the test cells were captured using CSASA sensor as well as the reference UHF disc sensor placed equidistance (200 mm) from the test cell. The sensors were connected to the two channels of the DSO using two identical low loss coaxial cables. Table 2 shows the minimum voltage required for initiating PDs when exciting the test cells individually. The inception voltage tabulated for each PD defect in Table 2 is an average of 10 measurements at 3 bar SF_6 gas pressure. It can be observed that the standard deviation is less than 1 kV for all three defect types. As PD events are random in nature, 200 PD signals were collected per defect for both sensors.

TABLE 2. Inception voltages for several PDs.

S. No	PD Defect	Inception voltage (kV)
1	Corona	11.2±0.72
2	Particle movement	8.6±0.8
3	Surface discharge	11.6±0.6

For measuring PRPD pattern for each PD defect type, the output of UHF sensors was connected to the signal analyser one at a time as shown in Figure 10(f). The signal analyser was operated in zero span mode with center frequency 1 GHz, as identified from the spectral content of the UHF signal.

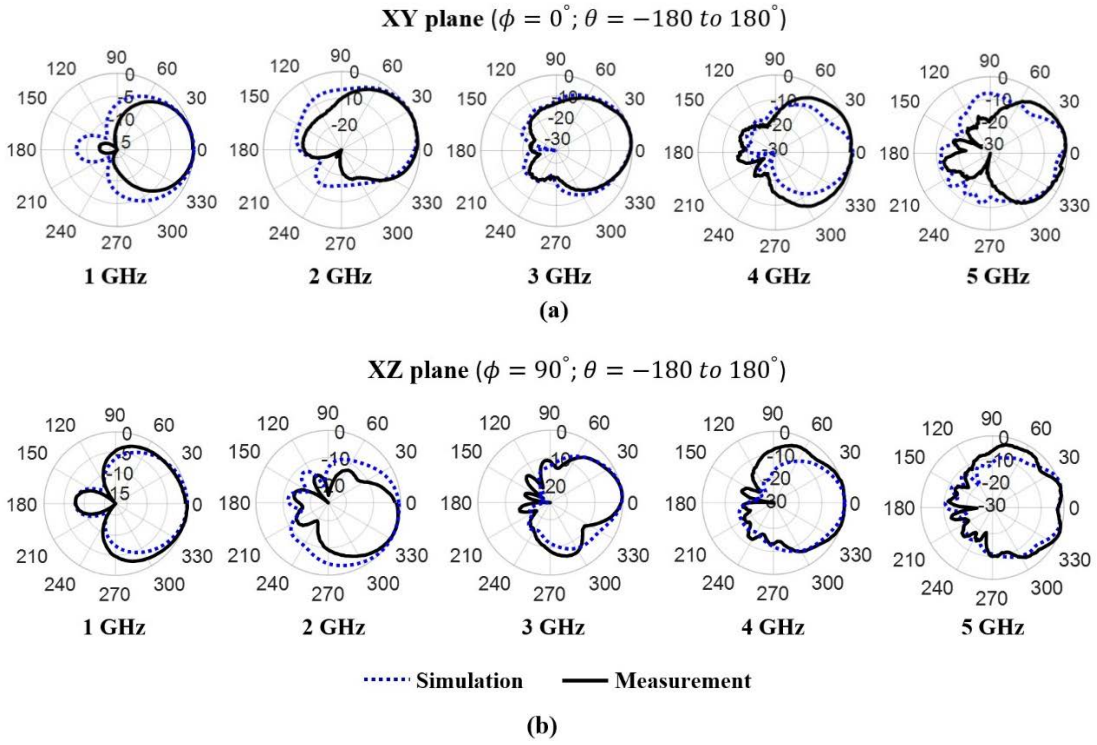

FIGURE 9. Radiation pattern of the UHF CSASA sensor in (a) E-plane (XY) and (b) H-plane (XZ).

Sinusoidal excitation with 25 cycles at 50 Hz and amplitude equal to the inception voltage was applied from function generator. Total 2000 sinusoid cycles were excited for each type of PD defect. The function generator and signal analyser were synchronized, and sweep time of 500 $ms(25 \times (1/50))$ was used in signal analyser which corresponds to burst with 25 cycles. The magnitude and time instances of the PDs initiated inside the test cells were recorded using signal analyser for the fabricated UHF CSASA and reference disc sensors.

B. RAW PD SIGNAL ANALYSIS

Figure 11 shows the sequence of raw PD signals captured by the CSASA UHF sensor for Cor, PM, and SD type of activities for the experimental setup in Figure 10(e). PD signals captured by reference disc sensor simultaneously for the three PD defects are also shown in Figure 11. It is observed that the both reference disc sensor and CSASA sensor detected all PD events, but the amplitude of PD signals detected by CSASA sensor is always higher than reference disc sensor for all PD signals. This is due to the fact that the CSASA sensor has positive gain throughout its operating frequency band. It is further noticed from Figures 11(b) and 11(e) that CSASA sensor even detected small PD signals that were not detected by reference disc sensor due to its better sensitivity. This confirms the ability of the CSASA sensor to detect all the PD events detected by the reference UHF PD sensor with a relatively higher signal strength compared to the reference sensor.

Figure 12 shows the time domain PD signals and their corresponding spectrum gathered using CSASA sensor and reference disc sensor for the three PD defects in the simulated GIS test cells. Figure 12 clearly shows higher signal strength and broader spectral content for the proposed UHF sensor in time and frequency domains, respectively when compared to the reference sensor. The raw PD signals clearly demonstrate that the UHF CSASA sensor has better PD detection sensitivity than the reference UHF PD sensor. Furthermore, the cost of the fabricated sensor is significantly lower than the commercial disc sensor used in this study for PD measurements.

C. PHASE RESOLVED PARTIAL DISCHARGE ANALYSIS

PRPD signals were collected for all the partial discharges presented above. PRPD analysis presents the magnitude of the PD and the phase at which the PD event occurred during the HV excitation in the power apparatus. This information is essential to determine the sensitivity of the UHF sensor to the PD event and validate the source of the PD event. Figure 13 shows the PRPD analysis of the UHF EM emissions due to Cor, PM and SD type of PDs in the GIS test cells gathered by the UHF CSASA and reference disc sensors. Each data point in Figure 13 measured by the UHF sensor using the signal analyzer represents the magnitude of PD event and phase at which it occurred. It can be observed that the PRPD plots has varying patterns for the three PD defects which demonstrate the sensitivity and PD detection capability of the proposed UHF sensor. The PRPD patterns

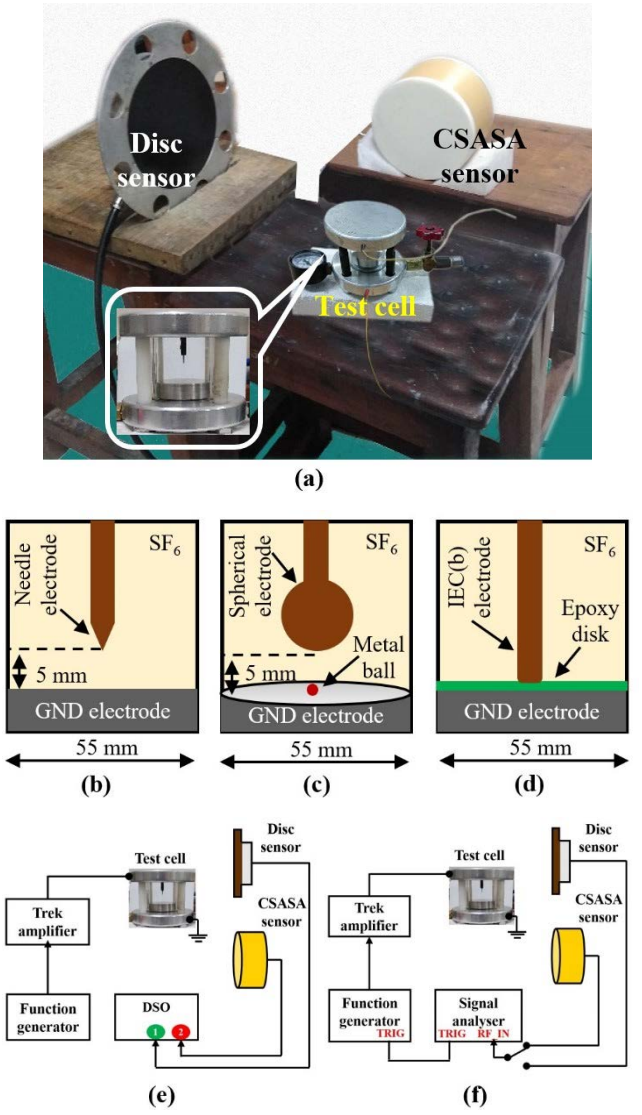

FIGURE 10. (a) Experimental setup for PD detection showing CSASA sensor, reference disc sensor and test cell; electrode configurations inside test cell for generating PDs of type (b) Corona, (c) particle movement, (d) surfaced discharge; Illustration of experimental setup for detecting (e) raw PD signals and (f) PRPD signals.

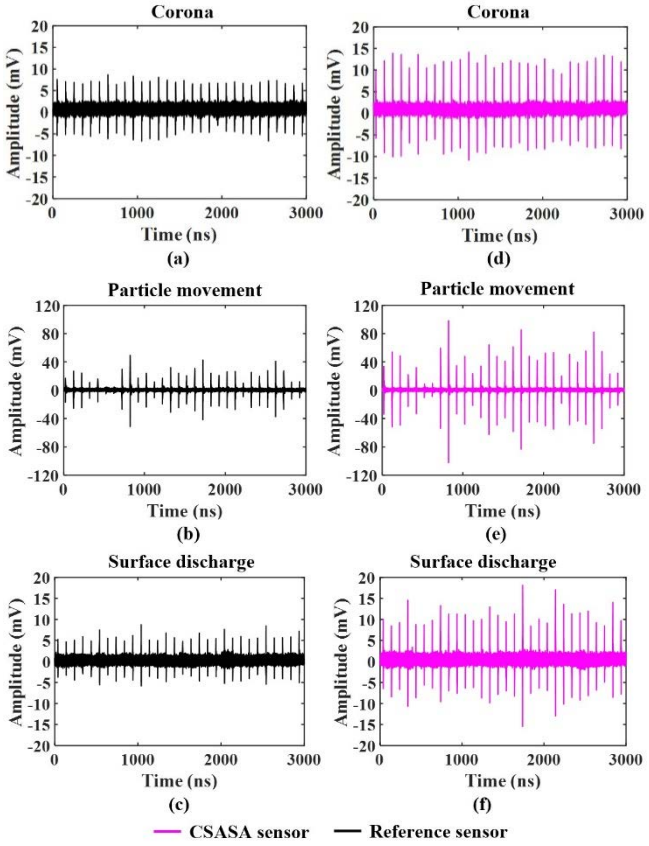

FIGURE 11. Measurement of PD signals. (a)-(c) Reference disc sensor and (d)-(f) CSASA sensor PD measurements for Corona, particle movement and surface discharge type of defects.

for the three PD defects in Figure 13 clearly indicate larger magnitude for the PRPD signals detected by UHF CSASA sensor than reference UHF disc sensor. Figure 13 (d) shows that Corona discharges occurred from 48 to 126° centered about 90° in the positive half cycle, and over 228 to 300° centered about 270° in the negative half cycle for the CSASA sensor. Secondary electron emission around the cathode is responsible for negative Corona discharges. Due to nonuniform electric field and space charge accumulation around the tip of protrusion, negative Corona discharges form around 270°. Positive corona discharges occur around 90° due to enhancement of the local electric field by accumulated positive charges around the cathode which enhance the electron avalanches and cause the discharges. The number of Corona discharges that occurred in positive half cycle and negative half cycle were 605 and 538, respectively for both UHF sensors. The discharge magnitude of positive and negative Corona discharges is almost similar as reported by Xian-Jun Shao *et al.* for protrusion defect on HV conductor in 252 kV GIS [25]. Ju Tang *et al.* simulated protrusion defect in test cell for PD severity assessment and observed similar PRPD pattern when PD intensity is at normal level [26].

PRPD pattern for PM type of PD activity occurred over the entire AC cycle in Figures 13(b) and 13(e). This behaviour is expected when a particle is dancing in the HV GIS test cell. Thus there is no obvious phase dependency in Figures 13(b) and 13(e) [25]. The frequency of PM type of PD discharges is about 407 in the positive and negative half cycles for both UHF sensors. The PD magnitude variation was relatively high for PM than the other two PD defects. Meijer *et al.* studied the free moving particles influence on the insulation strength in 380 kV GIS and observed similar PRPD pattern when the particle is dancing [27]. Minh-Tuan Nguyen *et al.* classified four types of PDs including particle movement by extracting features from their respective PRPD patterns, and reported similar observation for the PRPD pattern of PM defect [28].

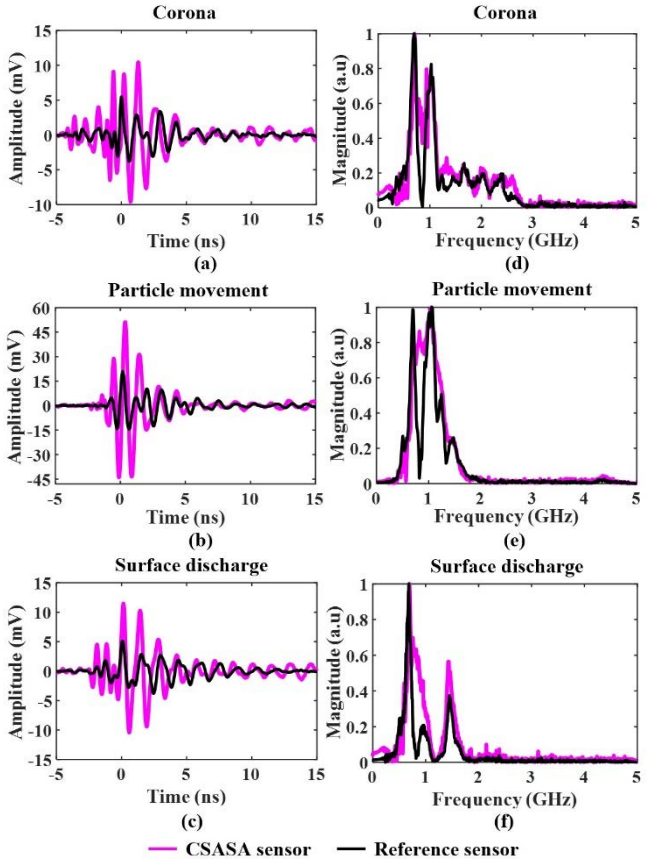

FIGURE 12. PD signal analysis. (a)-(c) Time domain signals and their (d)-(f) spectral magnitude for Corona, particle movement and surface discharge type of defects.

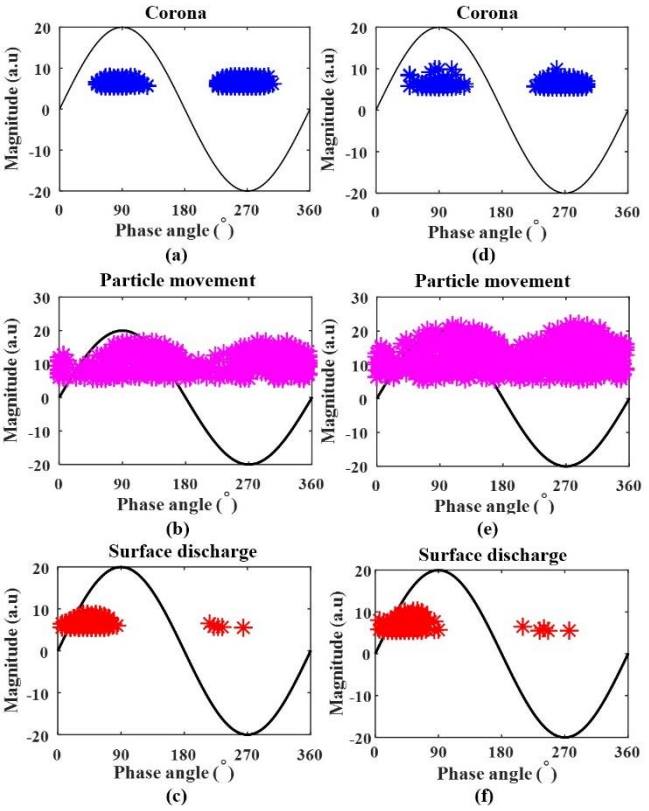

FIGURE 13. PRPD signal analysis. (a)-(c) Reference disc sensor and (d)-(f) CSASA sensor PD measurements for Corona, particle movement and surface discharge type of defects.

PRPD patterns of SD shown in Figures 13(c) and 13(f) indicate that SD type of discharges occurred mostly in the rising edge of the AC voltage with phase windows of 0 to 90° and 192 to 246° in the positive and negative cycles, respectively. The number of SD type of discharges that occurred in the positive and negative half cycles were 596 and 14, respectively, indicating that SD type of discharges occur mostly in the positive half cycle. As the applied voltage was slightly above the inception voltage to initiate SD process, the discharge activity was observed at the rising edge of the applied AC voltage. Sheema *et al.* studied the influence of SD type of PDs due to harmonic AC voltages on oil impregnated press board in power transformers and also reported similar observations in the PRPD pattern for SD defect [29].

D. COMPARISON WITH OTHER UHF SPIRAL SENSORS

Table 3 presents the comparison of the fabricated UHF CSASA sensor with existing UHF spiral sensors reported for PD detection. It can be observed that most of the PD sensors do not have electrical isolation which is essential for PD detection in HV environment. As the presence of the radome deteriorates the antenna performance, it was included in the numerical model during sensor design optimization. It is well known that the spectrum of PD signals varies in the UHF range depending on the dimensions and type of the PD defects, defect orientation and location, and properties of the medium [6]. Thus, UHF sensors used for PD detection should have wide fractional bandwidth. Table 3 indicates that the spiral UHF antennas reported for PD detection cover only a fraction of the desired spectrum and their size is also large compared to their operating bandwidth unlike the proposed UHF sensor. It should be noted that the smaller aperture size of the UHF spiral antenna reported in [16] is due to the higher operating bandwidth. The electrical size of the UHF CSASA sensor with the lower operating frequency of 0.5 GHz is the smallest ($0.26\lambda_L$) compared to the existing UHF spiral PD sensors. Aperture size miniaturization was possible due to cosine wave meandering of the spiral arms. It is also observed that the AR which is an indicator of circular polarization is not reported for most of the spiral UHF PD sensors [9], [13]–[18] except [10]. It can be observed that the proposed UHF CSASA sensor has the widest operating bandwidth in the UHF range with circular polarization when compared to spiral UHF sensors reported for PD detection. Furthermore, the proposed UHF sensor has a simple and miniaturized feed unlike the large ultrawideband balun feed used in the existing sensors. The proposed UHF sensor has unidirectional radiation pattern and positive gain in the operating bandwidth of 0.5 to 5 GHz due to the optimized cavity

TABLE 3. Comparison with UHF spiral antennas reported for PD detection.

Ref	−10 dB S_{11} Bandwidth (GHz)	Radiation pattern	Maximal dimension in mm (Electrical length)	Balun	Cavity height (mm)	< 3 dB Axial ratio bandwidth (GHz)	PD detection capability	PD defect types
[10]	0.6-1.7	Unidirectional	200 ($0.40\lambda_L$)	✓	153 (λ_L)	0.6-1.7	No	No
[16]	0.925-1.6	Unidirectional	95 ($0.30\lambda_L$)	✓	40 ($0.12\lambda_L$)	NA	No	No
[17]	0.5-1.5	Unidirectional	192 ($0.32\lambda_L$)	✓	80 ($0.13\lambda_L$)	NA	No	No
[13]	0.7-3	Bidirectional	218 ($0.50\lambda_L$)	✓	NA	NA	No	No
[9]	0.5-2.55	Bidirectional	283 ($0.48\lambda_L$)	×	NA	NA	Yes (GIS test cell)	Cor
[14, 15]	0.75-2	Unidirectional	202 ($0.50\lambda_L$)	✓	NA	NA	Yes†	-
[18]	0.8-3	Not presented	184 ($0.5\lambda_L$)	✓	NA	NA	Yes (GIS test cell)	Cor
*	0.5-5	Unidirectional	154 ($0.26\lambda_L$)	×	80 ($0.13\lambda_L$)	0.5-5	Yes (GIS test cell)	Cor, PM, SD

*: Present work; NA – not available

†: Repetitive impulse voltages with rise times changing from 50 ns-100 ns

backing. The optimized cavity height is electrically short compared to the existing spiral sensors considering the lower operating frequency of the UHF sensor. From Table 3, it is evident that the cavity backed UHF CSASA sensor with the radome reported in this work for PD detection has better radiation characteristics than the existing spiral UHF sensors. PD measurements reported for three commonly occurring PD defects in GIS test cells demonstrate PD detection capability with better sensitivity for the proposed UHF CSASA sensor than the reference UHF sensor. PD signal measurements of the proposed compact UHF CSASA sensor suggest that it could be used as an internal or external sensor for PD detection.

V. CONCLUSION

A CSASA sensor was designed for continuous detection of partial discharges in HV equipment. The sensor was designed to operate from 0.5–5 GHz with unidirectional radiation pattern and reduced aperture size (158 mm diameter). The sensor characteristics such as return loss, gain and radiation pattern measurements were in good agreement with the simulation results. The proposed CSASA UHF sensor is electrically smaller and has polarization purity over the ultrawideband bandwidth when compared to the existing UHF spiral antennas for PD detection. PD measurements indicate that the proposed CSASA sensor has the ability to detect the commonly occurring electrical discharges due to Corona, particle movement and surface discharge with 120% higher signal amplitude than the reference UHF disc sensor widely used for PD detection in GIS and power transformers. PRPD analysis confirms the PD detection capability with higher sensitivity for the CSASA sensor compared to the disc sensor. It is concluded that the proposed UHF sensor could be used for remote detection and monitoring of PDs occurring in HV electrical equipment such as GIS.

REFERENCES

[1] P. Bolin and H. Koch, "Gas insulated substation GIS," in *Proc. IEEE Power Eng. Soc. Gen. Meeting*, Montreal, QC, Canada, Jun. 2006, pp. 1–3.
[2] I. A. Metwally, "Status review on partial discharge measurement techniques in gas-insulated switchgear/lines," *Electr. Power Syst. Res.*, vol. 69, no. 1, pp. 25–36, 2004.
[3] Q. Khan, S. S. Refaat, H. Abu-Rub, and H. A. Toliyat, "Partial discharge detection and diagnosis in gas insulated switchgear: State of the art," *IEEE Elect. Insul. Mag.*, vol. 35, no. 4, pp. 16–33, Jul. 2019.
[4] G. C. Stone, "Partial discharge diagnostics and electrical equipment insulation condition assessment," *IEEE Trans. Dielectr. Electr. Insul.*, vol. 12, no. 5, pp. 891–904, Oct. 2005.
[5] M. D. Judd, L. Yang, and I. B. B. Hunter, "Partial discharge monitoring of power transformers using UHF sensors. Part I: Sensors and signal interpretation," *IEEE Elect. Insul. Mag.*, vol. 21, no. 2, pp. 5–14, Mar. 2005.
[6] A. Darwish, S. S. Refaat, H. A. Toliyat, and H. Abu-Rub, "On the electromagnetic wave behavior due to partial discharge in gas insulated switchgears: State-of-art review," *IEEE Access*, vol. 7, pp. 75822–75836, 2019.
[7] M. M. O. Harbaji, A. H. Zahed, S. A. Habboub, M. A. AlMajidi, M. J. Assaf, A. H. El-Hag, and N. N. Qaddoumi, "Design of Hilbert fractal antenna for partial discharge classification in oil-paper insulated system," *IEEE Sensors J.*, vol. 17, no. 4, pp. 1037–1045, Feb. 2017.
[8] C. Zachariades, R. Shuttleworth, and R. Giussani, "A dual-slot barrier sensor for partial discharge detection in gas-insulated equipment," *IEEE Sensors J.*, vol. 20, no. 2, pp. 860–867, Jan. 2020.

[9] C. Zachariades, R. Shuttleworth, R. Giussani, and T.-H. Loh, "A wideband spiral UHF coupler with tuning nodules for partial discharge detection," *IEEE Trans. Power Del.*, vol. 34, no. 4, pp. 1300–1308, Aug. 2019.
[10] S. Park and K. Y. Jung, "Design of a circularly-polarized uhf antenna for partial discharge detection," *IEEE Access*, vol. 8, pp. 81644–81650, 2020.
[11] Z. Huamao, L. Yazhou, and Z. Shusheng, "Study on the disc sensor based on the cavity mold theory," *IEEE Sensors J.*, vol. 16, no. 13, pp. 5277–5282, Jul. 2016.
[12] Y. R. Yadam, S. Ramanujam, and K. Arunachalam, "An ultrawideband conical monopole with radome for detection of partial discharges," *IEEE Sensors J.*, vol. 21, no. 17, pp. 18764–18772, Sep. 2021.
[13] T. Li, M. Rong, C. Zheng, and X. Wang, "Development simulation and experiment study on UHF partial discharge sensor in GIS," *IEEE Trans. Dielectr. Electr. Insul.*, vol. 19, no. 4, pp. 1421–1430, Aug. 2012.
[14] W. Zhou, P. Wang, Z. Zhao, Q. Wu, and A. Cavallini, "Design of an archimedes spiral antenna for PD tests under repetitive impulsive voltages with fast rise times," *IEEE Trans. Dielectr. Electr. Insul.*, vol. 26, no. 2, pp. 423–430, Apr. 2019.
[15] P. Wang, S. Ma, S. Akram, K. Zhou, Y. Chen, and M. T. Nazir, "Design of archimedes spiral antenna to optimize for partial discharge detection of inverter fed motor insulation," *IEEE Access*, vol. 8, pp. 193202–193213, 2020.
[16] J. Lee, J. Cho, J. Choi, H. Choo, and K.-Y. Jung, "Design of a miniaturized spiral antenna for partial discharge detection system," *Microw. Opt. Technol. Lett.*, vol. 60, no. 1, pp. 75–78, Jan. 2018.
[17] H.-B. Kim, K.-C. Hwang, and H.-S. Kim, "Cavity-backed two-arm spiral antenna with a ring-shaped absorber for partial discharge diagnosis," *J. Electr. Eng. Technol.*, vol. 8, no. 4, pp. 856–862, Jul. 2013.
[18] J. Liu, G. Zhang, J. Dong, and J. Wang, "Study on miniaturized UHF antennas for partial discharge detection in high-voltage electrical equipment," *Sensors*, vol. 15, no. 11, pp. 29434–29451, 2015.
[19] J. M. O'Brien, J. E. Grandfield, G. Mumcu, and T. M. Weller, "Miniaturization of a spiral antenna using periodic Z-plane meandering," *IEEE Trans. Antennas Propag.*, vol. 63, no. 4, pp. 1843–1848, Apr. 2015.
[20] H. Nakano, "A meander spiral antenna," in *Proc. IEEE Antennas Propag. Soc. Symp.*, Monterey, CA, USA, vol. 3, Jun. 2004, pp. 2243–2246.
[21] Z.-H. Song, S. Tian, and J.-H. Qiu, "The simulation and design of a meander Archimedean spiral antenna," in *Proc. IEEE Antennas Propag. Soc. Int. Symp.*, Albuquerque, NM, USA, Jul. 2006, pp. 3673–3676.
[22] C. Zhang, N. Hu, W. Yin, Y. Zhao, M. Lu, and Y. Wang, "A miniaturized planar spiral antenna for PD detection in GIS," in *Proc. IEEE 4th Conf. Energy Internet Energy Syst. Integr. (EI2)*, Wuhan, China, Oct. 2020, pp. 3302–3306.
[23] C. A. Balanis, "Frequency-independent antennas: Spirals and log-periodics," in *Modern Antenna Handbook*. Hoboken, NJ, USA: Wiley, 2011, pp. 281–300.
[24] C. A. Balanis, "Circular cross-section waveguides and cavities," in *Advanced Engineering Electromagnetics*, 2nd ed. Hoboken, NJ, USA: Wiley, 2012, pp. 500–508.
[25] X. Shao, W. He, J. Xu, M. Zhu, and G. Zhang, "Partial discharge detection by extracting UHF signal from inner grading electrode of insulating spacer in GIS," *IET Sci., Meas. Technol.*, vol. 12, no. 1, pp. 90–97, Jan. 2018.
[26] J. Tang, M. Jin, F. Zeng, S. Zhou, X. Zhang, Y. Yang, and Y. Ma, "Feature selection for partial discharge severity assessment in gas-insulated switchgear based on minimum redundancy and maximum relevance," *Energies*, vol. 10, no. 10, p. 1516, Oct. 2017.
[27] S. Meijer and J. J. Smit, "UHF defect evaluation in gas insulated equipment," *IEEE Trans. Dielectr. Electr. Insul.*, vol. 12, no. 2, pp. 285–296, Apr. 2005.
[28] M.-T. Nguyen, V.-H. Nguyen, S.-J. Yun, and Y.-H. Kim, "Recurrent neural network for partial discharge diagnosis in gas-insulated switchgear," *Energies*, vol. 11, no. 5, p. 1202, May 2018.
[29] R. Sarathi, I. P. M. Sheema, J. S. Rajan, and M. G. Danikas, "Influence of harmonic AC voltage on surface discharge formation in transformer insulation," *IEEE Trans. Dielectr. Electr. Insul.*, vol. 21, no. 5, pp. 2383–2393, Oct. 2014.

YUGANDHARA RAO YADAM received the M.S. degree from the Indian Institute of Technology (IIT) Madras, Chennai, India, in 2016, where he is currently pursuing Ph.D. degree with the Department of Engineering Design, working on design of UHF sensors and modeling partial discharge signal propagation in GIS.

RAMANUJAM SARATHI (Senior Member, IEEE) received the Ph.D. degree from the Indian Institute of Science, Bengaluru, in 1994. He is currently a Professor and the Head of the High Voltage Laboratory, Department of Electrical Engineering, IIT Madras, Chennai, India. His research interests include condition monitoring of power apparatus and nano materials.

KAVITHA ARUNACHALAM (Member, IEEE) received the Ph.D. degree from Michigan State University, East Lansing, USA, in 2007. She is currently a Professor and the Head of the Electromagnetic Research Laboratory, Department of Engineering Design, IIT Madras, Chennai, India. Her research interests include EM sensors and antennas for nondestructive material measurements, bio-electromagnetics, and EM material characterization.